

See discussions, stats, and author profiles for this publication at: <https://www.researchgate.net/publication/236071948>

# Magnetic Anisotropy of Cyanide-Bridged Core and CoreShell Coordination Nanoparticles Probed by X-ray Magnetic Circular Dichroism

ARTICLE in CHEMISTRY - A EUROPEAN JOURNAL · MARCH 2013

Impact Factor: 5.73 · DOI: 10.1002/chem.201203609 · Source: PubMed

CITATIONS

3

READS

34

8 AUTHORS, INCLUDING:



**Marie-Anne Arrio**

Pierre and Marie Curie University - Paris 6

67 PUBLICATIONS 1,701 CITATIONS

SEE PROFILE



**Edwige Otero**

SOLEIL synchrotron

41 PUBLICATIONS 846 CITATIONS

SEE PROFILE



**Philippe Saintavit**

French National Centre for Scientific Resea...

84 PUBLICATIONS 2,055 CITATIONS

SEE PROFILE



**Talal Mallah**

Université Paris-Sud 11

164 PUBLICATIONS 6,907 CITATIONS

SEE PROFILE

# Magnetic Anisotropy of Cyanide-Bridged Core and Core–Shell Coordination Nanoparticles Probed by X-ray Magnetic Circular Dichroism

Yoann Prado,<sup>[a]</sup> Marie-Anne Arrio,<sup>[b]</sup> Florence Volatron,<sup>[a]</sup> Edwige Otero,<sup>[c]</sup> Christophe Cartier dit Moulin,<sup>[d]</sup> Philippe Saintavit,<sup>[b]</sup> Laure Catala,<sup>[a]</sup> and Talal Mallah<sup>\*,[a]</sup>

**Abstract:** The local symmetry and local magnetic properties of 6 nm-sized, bimetallic, cyanide-bridged CsNiCr(CN)<sub>6</sub> coordination nanoparticles **1** and 8 nm-sized, trimetallic, CsNiCr(CN)<sub>6</sub>@CsCoCr(CN)<sub>6</sub> core–shell nanoparticles **2** were studied by X-ray absorption spectroscopy (XAS) and X-ray magnetic circular dichroism (XMCD). The measurements were performed at the Ni<sup>II</sup>, Co<sup>II</sup>, and Cr<sup>III</sup> L<sub>2,3</sub> edges. This study revealed the presence of distorted Ni<sup>II</sup> sites located on the particle surface of **1** that account for the uniaxial magnetic anisotropy ob-

served by SQUID measurements. For the core–shell particles, a combination of the exchange anisotropy between the core and the shell and the pronounced anisotropy of the Co<sup>II</sup> ions is the origin of the large increase in coercive field from 120 to 890 Oe on going from **1** to **2**. In addition, XMCD allows the relative orientation of the magnetic

moments throughout the core–shell particles to be determined. While for the bimetallic particles of **1**, alignment of the magnetic moments of Cr<sup>III</sup> ions with those of Ni<sup>II</sup> ions leads to uniform magnetization, in the core–shell particles **2** the magnetic moments of the isotropic Cr<sup>III</sup> follow those of Co<sup>II</sup> ions in the shell and those of Ni<sup>II</sup> ions in the core, and this leads to nonuniform magnetization in the whole nanoobject, mainly due to the large difference in local anisotropy between the Co<sup>II</sup> ions belonging to the surface and the Ni<sup>II</sup> ions in the core.

**Keywords:** coordination networks • core–shell structures • magnetic anisotropy • nanoparticles • transition metals

## Introduction

Bimetallic, cyanide-bridged nanocrystals that have the Prussian blue face-centered cubic (fcc) structure (Prussian blue analogues) were first reported by Mann and co-workers, who used reverse micelles as nanoreactors.<sup>[1,2]</sup> The development of other synthetic approaches led to a variety of nanoobjects based on cyanide-bridged networks with magnetic

and photomagnetic properties.<sup>[3–10]</sup> All of the reported approaches needed the presence of a chemical agent to confine the growth of the nanoobjects. We developed a different approach based on electrostatic stabilization leading to water-soluble nanoobjects with surfaces free from any protecting matter.<sup>[11]</sup> The surface of the nanoparticles of a given network could thus be used for epitaxial growth of another network leading to core–shell nanocrystals that may have different magnetic properties.<sup>[12]</sup> When the core and the shell show different magnetic behaviors, a synergy may emerge that deeply affects the magnetic behavior, such as the blocking temperature and the coercive field. Moreover, the interaction between a strongly anisotropic (ferro- or antiferromagnetic) and a weakly anisotropic ferromagnetic material can lead to an extra exchange anisotropy and the phenomenon of exchange bias or exchange hardening.<sup>[13–16]</sup> We have already shown that 12 nm nanoparticles made of 8 nm CsNi<sup>II</sup>Cr<sup>III</sup>(CN)<sub>6</sub> cores and CsCo<sup>II</sup>Cr<sup>III</sup>(CN)<sub>6</sub> shells of 2 nm thickness lead to a dramatic increase in the coercive field by an order of magnitude compared to that of the CsNi<sup>II</sup>Cr<sup>III</sup>(CN)<sub>6</sub> core.<sup>[12,17]</sup> Our nanoparticles have a complex local structure. Their bimetallic structure results from the interaction between hexacyanochromate(III) ions and divalent metal ions (Ni<sup>II</sup> and Co<sup>II</sup>). The environment of the Cr<sup>III</sup> ions is the same within the whole object, while the divalent ions may have different local surroundings: six nitrogen atoms of Cr(CN)<sub>6</sub> ions (MN<sub>6</sub>) and a mixture of nitrogen atoms and oxygen atoms of water molecules (MN<sub>6–x</sub>O<sub>x</sub>).

[a] Dr. Y. Prado, Dr. F. Volatron, Dr. L. Catala, Prof. Dr. T. Mallah  
Institut de Chimie Moléculaire et des Matériaux d'Orsay  
Université Paris-Sud 11, CNRS  
15 rue Georges Clemenceau, 91405 Orsay Cedex (France)  
E-mail: yoann.prado@gmail.com  
talal.mallah@u-psud.fr

[b] Dr. M.-A. Arrio, Dr. P. Saintavit  
Institut de Minéralogie et de Physique des Milieux Condensés, CNRS  
UMR 7590  
Université Pierre et Marie Curie  
4 place Jussieu, 75252 Paris cedex 05 (France)  
E-mail: marie-anne.arrio@impmc.upmc.fr

[c] Dr. E. Otero  
Synchrotron-SOLEIL  
L'Orme des Merisiers, 91192 Saint-Aubin (France)

[d] Dr. C. Cartier dit Moulin  
Institut Parisien de Chimie Moléculaire, CNRS UMR 7201  
Université Pierre et Marie Curie  
4 place Jussieu, 75252 Paris Cedex 05 (France)

Supporting information for this article is available on the WWW under <http://dx.doi.org/10.1002/chem.201203609>.

Furthermore, the distribution of the different surroundings of the metal ions within a nanoparticle is not known, even though one may reasonably assume that water molecules terminate those present at the surface.

The different local symmetries and electronic structures of the metal ions of the nanoobjects is expected to lead to a complex and rich magnetic behavior, mainly governed by the magnetic anisotropy of the metal ions. While octahedral  $\text{Cr}^{\text{III}}(\text{CN})_6$  is magnetically rather isotropic, hexacoordinate  $\text{Ni}^{\text{II}}(\text{d}^8)$  complexes may have appreciable magnetic anisotropy that can be of the Ising type for particular local symmetries.<sup>[18]</sup> For octahedral  $\text{Co}^{\text{II}}$  complexes, the magnetic anisotropy is usually of the XY type and, in most cases, is very large because of first-order (or near-first-order) spin–orbit coupling.<sup>[19]</sup> Since the magnetic anisotropy of these nanoobjects is mainly related to the magnetic anisotropy of the single metal ions, good knowledge of the local structure is of primary importance to unravel the effect of 1) the different metal ions, 2) metal ions of the same type but with different environments, and 3) metal ions of the same type present in the bulk, on the surface, and, for core–shell particles, at the interface between the two networks.

X-ray absorption spectroscopy (XAS) offers the possibility to investigate the local structure. The response of a given metal ion depends on its local symmetry, and different signals are expected for different local symmetries.<sup>[20]</sup> X-ray magnetic circular dichroism (XMCD) at the edge of each metal ion reveals the local magnetic contribution to the overall magnetic behavior and is particularly useful for the core–shell nanostructures, in which three different magnetic ions are present.<sup>[21–23]</sup>

In this work, we used XAS and XMCD at the  $L_{2,3}$  edges of  $\text{Ni}^{\text{II}}$ ,  $\text{Cr}^{\text{III}}$ , and  $\text{Co}^{\text{II}}$  to investigate the local structure and the element-dependent magnetism of 6 nm  $\text{CsNi}^{\text{II}}\text{Cr}^{\text{III}}(\text{CN})_6$  nanoparticles **1** and 8 nm  $\text{CsNi}^{\text{II}}\text{Cr}^{\text{III}}(\text{CN})_6@\text{CsCo}^{\text{II}}\text{Cr}^{\text{III}}(\text{CN})_6$  core–shell nanoparticles **2** made from a core of **1** surrounded by a 1 nm shell of the  $\text{CsCo}^{\text{II}}\text{Cr}^{\text{III}}(\text{CN})_6$  network. We show the existence of distorted  $\text{Ni}^{\text{II}}$  sites, which deviate from  $O_h$  symmetry and are localized on the surface and in the bulk of the particles. The  $\text{Ni}^{\text{II}}$  sites at the surface induce a surface anisotropy that accounts for the magnetic anisotropy of these particles. For the core–shell particles, the large anisotropy due to the presence of  $\text{Co}^{\text{II}}$  in the shell (interface and surface) in addition to the exchange anisotropy associated with the core–shell architecture induces an overall larger magnetic anisotropy and more importantly leads to nonuniform magnetization in the core–shell nanoobjects.

## Results and Discussion

**Characterization of the products:** The synthetic procedure for the 6 nm  $\text{CsNi}^{\text{II}}\text{Cr}^{\text{III}}(\text{CN})_6$  nanoparticles have been already reported by some of us.<sup>[4,11]</sup> We prepared the core–shell nanoparticles by applying the same procedure reported in 2009 by some of us to similar nanocrystals.<sup>[12]</sup> It consists of the growth of the bimetallic, cyanide-bridged

$\text{CsCo}^{\text{II}}\text{Cr}^{\text{III}}(\text{CN})_6$  network on top of the 6 nm  $\text{CsNi}^{\text{II}}\text{Cr}^{\text{III}}(\text{CN})_6$  nanoparticles in water. A relatively low concentration of the  $\text{K}_3[\text{Cr}^{\text{III}}(\text{CN})_6]$  and  $[\text{Co}(\text{H}_2\text{O})_6]\text{Cl}_2$  precursors was used to preclude side nucleation of the  $\text{CsCo}^{\text{II}}\text{Cr}^{\text{III}}(\text{CN})_6$  nanoparticles during the process. Since the two networks have almost the same cell parameters (the ionic radii of  $\text{Ni}^{\text{II}}$  and  $\text{Co}^{\text{II}}$  differ very little), epitaxial growth is realized. Assuming a perfect growth process in solution, it is straightforward to estimate the amount of material required to grow a shell with a given thickness if the structure, cell parameters, and size of the seed nanoparticles (6 nm  $\text{CsNi}^{\text{II}}\text{Cr}^{\text{III}}(\text{CN})_6$  here) are known. Details of the calculation are given in the Supporting Information. Dynamic light scattering (DLS) measurements give the hydrodynamic diameters of the two types of nanocrystals in solution, but slightly overestimates the size of the objects. Sizes around 7 and 10 nm were measured for the  $\text{CsNi}^{\text{II}}\text{Cr}^{\text{III}}(\text{CN})_6$  and core–shell particles, respectively, as expected. More importantly, observation of only one peak for the core–shell nanoobjects confirmed the absence of any other type of nanoobjects in solution and supported the occurrence of a growth process without side nucleation. These negatively charged water–“soluble” nanoparticles were then isolated by using the cationic surfactant dioctadecyl dimethylammonium ( $\text{DODA}^+$ ) to give compounds **1** and **2** (see Experimental Section).<sup>[11]</sup> For a nanocrystal made of 1 nm-thick shell grown on a 6 nm core, the calculated amounts of material for the shell and the core are almost the same. Elemental analysis (see Experimental Section) confirms this prediction, and again indicates a perfect growth process.

The asymmetric vibrational band of the cyanide bond occurs in the 2000–2200  $\text{cm}^{-1}$  region of the IR spectrum. The bands observed at 2127  $\text{cm}^{-1}$  (see Figure S2 in the Supporting Information) correspond to terminal cyanide bonds and are associated with  $\text{Cr}(\text{CN})_6^{3-}$  ions located on the surface of the particles. The bands observed at 2172 and 2169  $\text{cm}^{-1}$  for **1** and **2**, respectively, are assigned to bridging cyanide ligands in the bulk of the particles. The slight energy difference observed is expected, since the bridging cyanide molecules belonging to the bimetallic network containing  $\text{Co}^{\text{II}}$  have a lower vibrational energy than those of the  $\text{Ni}^{\text{II}}$  network.

The X-ray powder diffraction patterns in the 15–60° range are consistent with a face-centered cubic structure (see Figure S3 in the Supporting Information).<sup>[24,25]</sup> The lattice parameter increases from  $a = 10.49 \text{ \AA}$  for **1** to  $a = 10.55 \text{ \AA}$  for **2**; the  $\text{CsCo}^{\text{II}}\text{Cr}^{\text{III}}(\text{CN})_6$  network has a slightly larger lattice constant than the  $\text{CsNi}^{\text{II}}\text{Cr}^{\text{III}}(\text{CN})_6$  network. The half-width of the Bragg reflections decreases on going from **1** to **2**. On the basis of the small extra broadening due to the difference in lattice parameters of the two networks, a size of 9 nm was obtained for **2** by applying the Scherrer equation to the Bragg reflection (400), in good agreement with the expected value. A size of 6 nm was found for **1**.

Nanoparticles of **1** have already been characterized by TEM with dark-field imaging. These studies showed cubic particles that are slightly elongated in one direction with an

aspect ratio of 1.6.<sup>[4]</sup> TEM imaging of a dispersion of nanoparticles of **2** in dichloromethane shows well-faceted particles with a distribution centered at  $(8 \pm 2)$  nm, in good agreement with the expected size (Figure 1).

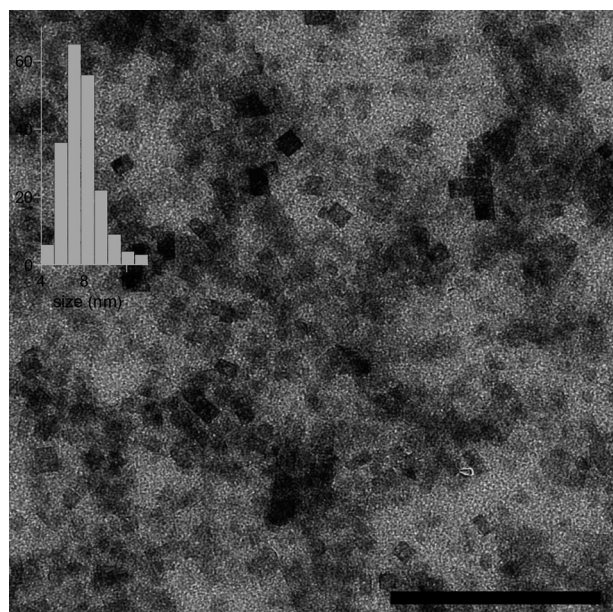


Figure 1. TEM image of nanocrystals of **2** obtained on redispersion in  $\text{CH}_2\text{Cl}_2$  of the particles embedded with  $\text{DODA}^+$  surfactant (scale bar: 100 nm). Inset: size distribution obtained from 200 observed nanoparticles.

**SQUID and XMCD studies on 1:** *SQUID magnetic measurements:* Alternating-current susceptibility measurements were performed in zero applied dc field and 3.5 Oe oscillating field at six different frequencies from 1 to 1000 Hz (see Figure S4 in the Supporting Information). The temperature dependence of the out-of phase signal shows a maximum around 50 K that is almost frequency-independent, at least between 1 Hz and 1 kHz. This is in line with ferromagnetic behavior of **1** with dipolar interactions between the nanocrystals. Indeed, we have already demonstrated that, when the nanoparticles are well diluted in an organic matrix or as monolayer on a surface, superparamagnetic behavior is observed with blocking of the magnetization below  $T_B = 4$  K.<sup>[26–27]</sup> Since the hydrocarbon tails of the  $\text{DODA}^+$  surfactant is estimated to be around 1 nm long, we expect the presence of dipolar interactions because of the short distance between the magnetic particles.

The magnetization curves  $M(H)$  of **1** recorded at 2 K (Figure 2) show hysteretic behavior with a coercive field of 120 Oe (cf. 47 Oe for the isolated particles). The magnetic moment at 5 T is  $3.91\mu_B$ , and this amounts to only 77 % of what would be expected for a full alignment of the magnetic moments due to the ferromagnetic exchange coupling between  $\text{Cr}^{\text{III}}$  and  $\text{Ni}^{\text{II}}$  through the cyanide bridge ( $4.95\mu_B$ ).<sup>[28,29]</sup> The exchange coupling parameter between the

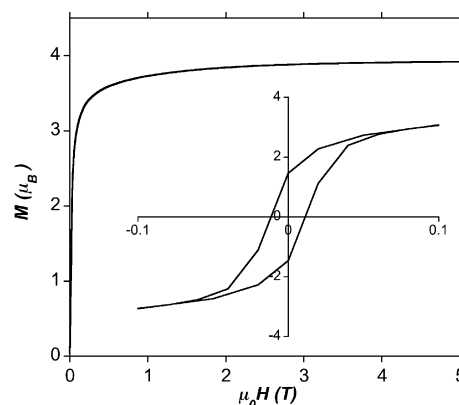


Figure 2. SQUID measurements of magnetization  $M(H)$  of **1** at 2 K.

$\text{Cr}^{\text{III}}$  and the  $\text{Ni}^{\text{II}}$  ions through the cyanide bridge was estimated to be in the range of  $15\text{--}20\text{ cm}^{-1}$ .<sup>[30–32]</sup>

**XAS and XMCD at the  $\text{Ni}^{\text{II}}$  and  $\text{Cr}^{\text{III}}$   $L_{2,3}$  edges:** The XMCD and the isotropic spectra ( $\sigma_{\text{xmcd}}$  and  $\sigma_{\text{iso}}$ , respectively) at the  $\text{Ni}^{\text{II}}$  and  $\text{Cr}^{\text{III}}$   $L_{2,3}$  edges for **1** were recorded at 4.2 K in an applied field of 2 T. From Figure 2, the magnetization per formula unit at 2 K is  $3.86\mu_B$ , since we do not expect temperature dependence between 2 and 4.2 K. The experimental spectra (Figure 3) are in close agreement with those obtained previously on bulk compounds.<sup>[28,33]</sup> Nevertheless, some differences appear in the experimental spectra of **1**

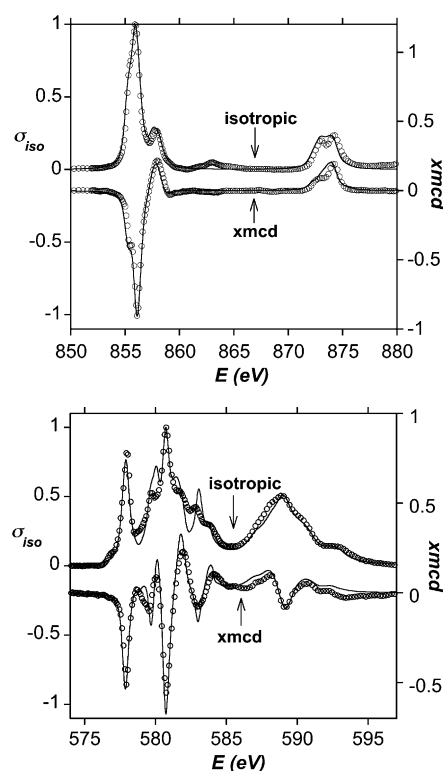


Figure 3. Experimental ( $\circ$ ) and theoretical (—) isotropic spectra and XMCD signal of **1** at the  $\text{Ni}^{\text{II}}$  (top) and the  $\text{Cr}^{\text{III}}$  (bottom)  $L_{2,3}$  edges ( $T = 4.2$  K,  $\mu_0 H = 2$  T).



compared to that of the bulk compound. At the  $\text{Ni}^{\text{II}}$   $L_{2,3}$  edge, the main peaks of  $\sigma_{\text{xmcd}}$  and  $\sigma_{\text{iso}}$  have shoulders at 855 eV (Figure 4), which are present neither in the spectrum

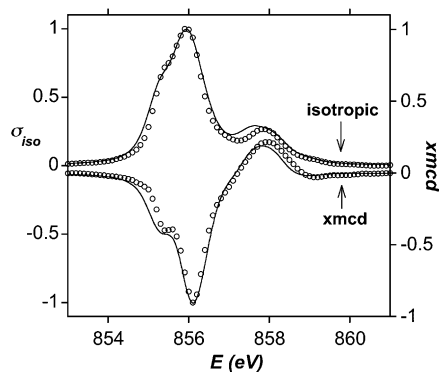


Figure 4. Experimental (○) and calculated (—) isotropic and XMCD spectra at the  $\text{Ni}^{\text{II}}$   $L_3$  edges for **1**.

of the bulk compound nor in the ligand field multiplet (LFM) calculations when  $O_h$  symmetry around the  $\text{Ni}^{\text{II}}$  ion is considered. This feature cannot be attributed to the diamagnetic species  $\text{Ni}^{\text{II}}(\text{CN})_4^{2-}$ , which could result from partial degradation of the sample. Indeed, the  $L_3$  edge of  $\text{Ni}^{\text{II}}(\text{CN})_4^{2-}$  appears at higher energy ( $> 856$  eV) in the isotropic spectrum, and  $\text{Ni}^{\text{II}}(\text{CN})_4^{2-}$  would not contribute to the XMCD signal. Accordingly, the  $\text{Ni}^{\text{II}}$  ions responsible for this shoulder are magnetic. We explain the features at 855.5 eV by the presence of  $\text{Ni}^{\text{II}}$  ions in a site with symmetry lower than  $O_h$ .

The occurrence of low-symmetry  $\text{Ni}^{\text{II}}$  ions could be explained by the presence of one or more water molecules in a coordination sphere of type  $\text{Ni}^{\text{II}}(\text{NC})_{6-x}(\text{OH}_2)_x$ . For 6 nm nanoparticles with perfect cubic shape, about 40% of the  $\text{Ni}^{\text{II}}$  ions are located on the surface of the particles (see Supporting Information for details of the calculations) and thus have the  $\text{Ni}^{\text{II}}(\text{NC})_5(\text{H}_2\text{O})$  coordination sphere, with the water molecule pointing out from the surface. In addition, distorted sites can be present in the volume of the particles and not only on the surface. Indeed, elemental analysis gives a Cr/Ni ratio of 0.92 corresponding to 8% vacancy of  $\text{Cr}(\text{CN})_6^{3-}$  ions in the nanocrystals. Each missing  $\text{Cr}(\text{CN})_6^{3-}$  ion must be compensated by six water molecules leading to six  $\text{Ni}^{\text{II}}$  distorted sites, as depicted by the red atoms in Figure 5 (top). Thus, it is likely that sites other than those located at the surface of the nanoparticles are distorted. Indeed, it was recently shown by solid-state NMR spectroscopy that such sites are present in the Prussian blue structure and that the proportion of the  $\text{Ni}(\text{NC})_4(\text{H}_2\text{O})_2$  sites is larger than is expected from a mere statistical distribution.<sup>[34–35]</sup> One can assume two extreme cases in which the vacancies associated with the missing  $\text{Cr}(\text{CN})_6^{3-}$  ions are either located homogeneously within the whole nanoparticles or only within the volume of the nanoparticles, excluding their surface. According to these assumptions, one finds

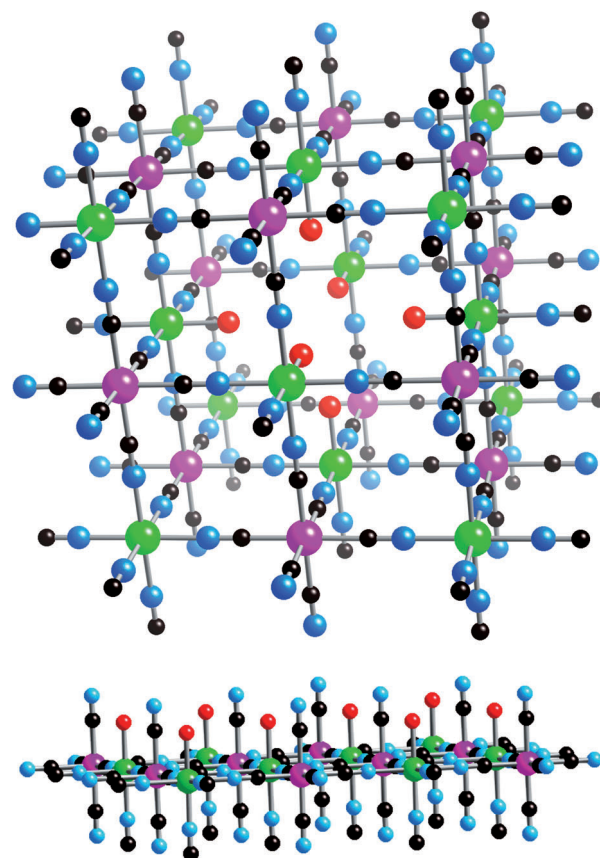


Figure 5. View of a cube of 1 nm size highlighting the  $\text{Cr}(\text{CN})_6$  vacancy and the water molecules (red) coordinated to the surrounding Ni atoms (top) and view of  $\text{Ni}-\text{OH}_2$  bonds normal to the particle surface (bottom). N blue, C black, Ni green, Cr pink.

that the proportion of  $\text{Ni}^{\text{II}}$  ions sitting in undistorted octahedral sites is  $(31 \pm 7)\%$ . Then the proportion of  $\text{Ni}^{\text{II}}$  ions in a distorted environment is  $(69 \pm 7)\%$  (see Supporting Information for details of the calculations).

Hence, the experimental spectra were fitted by taking into consideration  $\text{Ni}^{\text{II}}$  ions with octahedral symmetry ( $10Dq = 1.4$  eV) and  $\text{Ni}^{\text{II}}$  sites with a lower symmetry. For the sake of simplicity, the distorted  $\text{Ni}^{\text{II}}$  sites were considered to have  $D_{4h}$  symmetry and values of  $10Dq = 1$  eV and  $D_s = 0.2$  were taken for the calculations,<sup>[36]</sup> where  $10Dq$  is the energy difference between the triply and the doubly degenerate  $t_{2g}$  and  $e_g$  orbitals of the  $O_h$  sites, and  $D_s$  expresses the symmetry lowering from  $O_h$  to  $D_{4h}$ .<sup>[37]</sup> A positive  $D_s$  value corresponds to compression of the octahedron. With this set of parameters, the lowest-lying singly degenerate level with  $a_1(D_{4h})-t_{2g}(O_h)$  symmetry is separated by 1.4 eV from the twofold degenerate level with  $e(D_{4h})-e_g(O_h)$  symmetry. We performed the calculations with 100% circularly polarized light at  $T = 4$  K. A good agreement is found between the experimental and the calculated spectra by considering 69% of sites with  $D_{4h}$  symmetry and 31% with  $O_h$  symmetry. The calculated spectra were multiplied by a coefficient ( $k = 0.75$  and  $0.7$  for the  $\text{Ni}^{\text{II}}$  and  $\text{Cr}^{\text{III}}$  edges, respectively) to reproduce the intensity of the experimental spec-

tra (Figures 3 and 4). The fact that the reduction coefficients are mainly the same is a first indication of the alignment of one subnetwork relative to the other (see below).

The fraction of sites with  $D_{4h}$  symmetry (69%) needed to obtain a reasonable fit is in good agreement with the calculated number of distorted  $\text{Ni}^{\text{II}}$  sites of  $(69 \pm 7)\%$  (see Supporting Information). Calculations considering  $O_h$  and  $D_{4h}$  symmetry with negative  $D_s$  were carried out, but a good fit of the experimental data could not be obtained in either case.

According to LFM calculations, the  $D_{4h}$  sites are octahedra compressed along the fourfold axis, since the best fit is obtained for a positive  $D_s$  value. An axial compression of coordination sphere of  $\text{Ni}^{\text{II}}$  complexes having a spin of  $S=1$  results in stabilization of the  $M_s = \pm 1$  sublevels relative to  $M_s = 0$ <sup>[38–40]</sup> and leads to a nonzero value of the  $z$  component  $L_z$  of the orbital kinetic momentum and thus a local easy axis of magnetization collinear with the distortion axis. Thus, because the majority, if not all, of the  $\text{Ni}^{\text{II}}$  sites located on the surface of the particles have their  $\text{Ni}-\text{OH}_2$  bonds pointing out from the surface, the easy axis of magnetization is normal to the surface and thus to the faces of the cubic nanoobjects (Figure 5, bottom).<sup>[41]</sup> The deviation between the calculated and experimental spectra at the  $\text{Cr}^{\text{III}}$  edge is small and in line with what is found for XAS simulation of metalocyanides, so that there is no need to assume any distorted environment. This is indeed what one would expect, since the coordination sphere of the  $\text{Cr}^{\text{III}}$  ion is a rigid octahedron with six apical cyanide ligands.

In summary, the experimental XAS and XMCD data evidence the presence of a tetragonal distortion on the  $\text{Ni}^{\text{II}}$  sites located in the bulk and at the surface of the particles, the easy axis of magnetization of the  $\text{Ni}^{\text{II}}$  ions at the surface is normal to the faces of the nanoparticles, while the  $\text{Cr}^{\text{III}}$  ions are rather structurally isotropic, as expected. The LFM calculations give valuable insight into the overall magnetic anisotropy. Indeed, the LFM calculations were carried out for the local magnetic moments fully aligned with the magnetic field. The need to apply a reduction coefficient to reproduce the intensity of the experimental intensity of the XMCD spectra and the fact that the coefficients are mainly the same for the two edges suggests that 1) the magnetic moments within the particles are not fully aligned with the magnetic field, which can be due to the surface anisotropy, as an easy axis of magnetization normal to the faces of the particles was found, and 2) the  $\text{Cr}^{\text{III}}$  and  $\text{Ni}^{\text{II}}$  networks are aligned relative to one other, which indicates that the magnetization of the structurally isotropic network ( $\text{Cr}^{\text{III}}$ ) follows that of the anisotropic one ( $\text{Ni}^{\text{II}}$ ). This results from the relatively strong ferromagnetic exchange coupling between the  $\text{Cr}^{\text{III}}$  and  $\text{Ni}^{\text{II}}$  ions through the cyanide bridge.<sup>[30–32]</sup>

To gain further insight into the magnetization state localized on each ion and, in particular, of the overall magnetic anisotropy of **1**, we studied the behavior of the magnetization as a function of the applied field at the two edges.

**Magnetization curves: variation of the  $\text{Ni}^{\text{II}}$  and  $\text{Cr}^{\text{III}}$  local magnetic moments with magnetic field:** We measured XMCD-detected magnetization curves at 4.2 K. To this end, one sets the monochromator at a fixed energy at which XMCD is the largest (i.e., 852.2 eV for the  $\text{Ni}^{\text{II}}$  and 574.5 eV for the  $\text{Cr}^{\text{III}}$  edge) and measures  $\sigma_L(B)$  and  $\sigma_R(B)$  while the applied external magnetic field  $B$  follows a cycle from +5 T to –5 T and back. Since the shape of the XMCD spectrum is independent on the external magnetic field, measuring the variation of XMCD at one energy is strictly equivalent to recording a magnetization curve. When applied to the XMCD spectra of Figure 3, the orbit and spin magneto-optic sum rules yield the atomic total magnetic moment (i.e., the sum of orbit and spin magnetic moments) at 2 T.

To express the experimental magnetization curves in Bohr magnetons, each value was normalized by the theoretical magnetization with full alignment to give a rate of magnetization. This was multiplied by the calculated total magnetic moment  $M_T$  ( $M_T = M_L + M_S$ , where  $M_L$  and  $M_S$  are the orbital and spin magnetic moments, respectively). In the case of the  $\text{Ni}^{\text{II}}$   $L_{2,3}$  edge, the two different symmetries ( $O_h$  and  $D_{4h}$ ) were considered, as the orbital magnetic moments differ. Taking into account the relative quantities of the two  $\text{Ni}^{\text{II}}$  environments ( $x_{O_h}$  and  $x_{D_{4h}}$ ) and the different values of the orbital component ( $\langle L_z \rangle_{O_h}$  and  $\langle L_z \rangle_{D_{4h}}$ ), the total orbital magnetic moment is expressed as Equation (1)

$$M_L = \langle L_z \rangle \mu_B = -[x_{O_h} \langle L_z \rangle_{O_h} + x_{D_{4h}} \langle L_z \rangle_{D_{4h}}] \mu_B \quad (1)$$

The values obtained from LFM calculations were used for normalization, that is,  $\langle L_z \rangle_{O_h} \approx -0.23$  and  $\langle L_z \rangle_{D_{4h}} \approx -0.32$ . The same value of the spin component was used for both symmetries ( $\langle S_z \rangle \approx -1$ ), leading to the spin magnetic moment  $M_S = -2 \langle S_z \rangle \mu_B$ . This leads to a magnetization of  $2.29 \mu_B$  for  $\text{Ni}^{\text{II}}$  corresponding to full alignment of the moments and taking into account the computed values for  $x_{O_h}$  and  $x_{D_{4h}}$  of 0.3 and 0.7, respectively. In the case of the  $\text{Cr}^{\text{III}}$   $L_{2,3}$  edge, the orbital moment is close to zero and the total moment is mainly due to the spin contribution ( $\langle S_z \rangle \approx -3/2$ ).

The local magnetization curves at 4.2 K show no evidence for hysteretic behavior (Figure 6), as the magnetic field step used between two consecutive measurements was larger (50 mT) than the coercive field of the sample (12 mT) obtained from SQUID measurements. At fields larger than 1 T, the slopes of the curves indicate that saturation is not achieved for  $\text{Ni}^{\text{II}}$  and  $\text{Cr}^{\text{III}}$  even at 5 T. The magnetization values at 5 T are  $1.86 \mu_B$  and  $2.33 \mu_B$  for  $\text{Ni}^{\text{II}}$  and  $\text{Cr}^{\text{III}}$  ions, respectively, which correspond to 81% ( $1.86/2.29$ ) and 78% ( $2.33/3$ ), respectively, of the maximum value expected for a full alignment of the local moments with the 5 T applied magnetic field. Since the shapes of the magnetization curves are nearly the same for both ions, we can conclude that the local magnetic moment of  $\text{Cr}^{\text{III}}$  follows that of  $\text{Ni}^{\text{II}}$  as the field is increased, and they do not deviate from each other. The sum of local magnetization curves of  $\text{Ni}^{\text{II}}$  and  $\text{Cr}^{\text{III}}$ , computed by considering the unit formula  $\text{NiCr}_{0.92}$ , led to the total magnetization curve shown in Figure 6. A value of

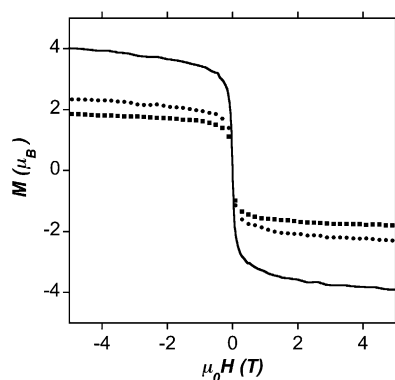


Figure 6. Local magnetization curves at 4.2 K at the Ni<sup>II</sup> (■) and Cr<sup>III</sup> (●) L<sub>2,3</sub> edges for **1** and reconstruction of the total magnetization (—) considering the formula Ni<sup>II</sup>[Cr<sup>III</sup>(CN)<sub>6</sub>]<sub>0.92</sub> (see text for details).

3.96 μ<sub>B</sub> was obtained at 5 T, in good agreement with the value obtained from SQUID measurements (3.91 μ<sub>B</sub>).

However, the XMCD magnetization curve reaches the maximum magnetization more gradually than that obtained by SQUID measurements. This difference may originate from the sensitivity of the XMCD technique to the surface. Indeed, the 6 nm nanoparticles are entirely probed but with weighted detection leading to a higher contribution of the ions located at the surface to the entire XMCD signal. Hence, taking into account the surface anisotropy normal to the faces of the cubic particles, the magnetic moments of ions at the surface are more difficult to orient in the field than those belonging to the volume of the particles, and this leads to weaker magnetization in the XMCD curve for weak applied field.

Both XAS and XMCD are local spectroscopic techniques that probe the local symmetry and the magnetic moments of the Ni<sup>II</sup> and Cr<sup>III</sup> networks, while SQUID is a bulk technique. The very good agreement between the XMCD and the SQUID magnetization data is evidence for the validity of our hypothesis that the local environment of the Ni<sup>II</sup> ions belonging to the surface is responsible for the magnetic anisotropy of **1**. An additional source of magnetic anisotropy may be dipolar interactions.<sup>[42–43]</sup> Indeed, SQUID studies on perfectly isolated particles of **1** gave a coercive field of 40 Oe, while in the present case, in which the particles are in close vicinity separated by the DODA<sup>+</sup> cations, the coercive field is 120 Oe.

**SQUID and XMCD studies on 2:** *SQUID magnetic measurements:* The  $\chi'' = f(T)$  curves for **2** display maxima around 40 K (see Supporting Information Figure S5) with almost no frequency dependence. We checked that particles diluted in polyvinylpyrrolidone have maxima at lower temperature (ca. 20 K) with some frequency dependence. This is a sign of the presence of strong dipolar interaction in **2**, as found for **1**. More importantly, only one maximum is found in the  $\chi'' = f(T)$  curves, which is the signature of a unique magnetic behavior of the nanocrystals of **2** despite the core-shell architecture. The temperature of the maximum (40 K) is lower

than that found for **1** (53 K) because the exchange coupling interactions within the CsCoCr(CN)<sub>6</sub> shell between Cr<sup>III</sup> and Co<sup>II</sup> through the cyanide bridge that contribute to 55% of the nanoobjects are weaker than those between Cr<sup>III</sup> and Ni<sup>II</sup> within the CsNiCr(CN)<sub>6</sub> core.<sup>[32,44,45]</sup>

The magnetization curve of **2** as a function of the magnetic applied field at 2 K (Figure 7) shows a hysteretic behavior with a coercive field of 890 Oe, larger than that observed for

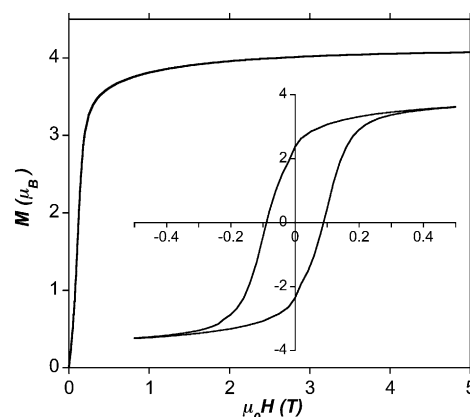


Figure 7. Magnetization curves  $M(H)$  at 2 K of **2**.

**1.** A value of 4.07 μ<sub>B</sub> is obtained for the magnetization at 5 T, which represents a saturation rate of 75% when the formula unit Ni<sub>0.51</sub>Co<sub>0.49</sub>Cr<sub>0.9</sub> with  $g_{\text{Ni}} = 2.2 = g_{\text{Co}}$ , and  $g_{\text{Cr}} = 1.99$  is taken into account. The exchange coupling parameter between the Co<sup>II</sup> and Cr<sup>III</sup> ions is relatively weak and can be estimated to be less than 7 cm<sup>-1</sup> from the  $T_{\text{C}}$  value of the bulk CsCoCr(CN)<sub>6</sub> compound,<sup>[45,46]</sup> while the magnetic anisotropy of Co<sup>II</sup> ions is very large because of the near-first-order spin-orbit coupling of hexacoordinate complexes. Thus, while for the CsNiCr(CN)<sub>6</sub> network the exchange field is dominant, for CsCoCr(CN)<sub>6</sub> the anisotropy field predominates.

*XAS and XMCD signals at the Ni<sup>II</sup>, Co<sup>II</sup>, and Cr<sup>III</sup> L<sub>2,3</sub> edges:* The XMCD ( $\sigma_{\text{XMCD}}$ ) and isotropic ( $\sigma_{\text{ISO}}$ ) spectra at the Ni<sup>II</sup>, Co<sup>II</sup>, and Cr<sup>III</sup> L<sub>2,3</sub> edges for **2** were recorded under the same conditions as for **1** ( $T = 4.2$  K,  $\mu_0 H = 2$  T; Figure 8 and Supporting Information Figure S6). In this case, the spectra calculated by the LFM method fit the experimental ones when they are multiplied by 0.7, 0.6, and 0.4 at the Ni<sup>II</sup>, Cr<sup>III</sup>, and Co<sup>II</sup> L<sub>2,3</sub> edges, respectively. The decrease corresponding to Co<sup>II</sup> is the largest and indeed indicates the large magnetic anisotropy of these ions, as expected from first-order spin-orbit coupling of their <sup>4</sup>T<sub>1g</sub> spectroscopic ground term. The different coefficients for the three different ions indicate that the magnetic moments of the less anisotropic ions (Ni<sup>II</sup> and Cr<sup>III</sup>) are not fully aligned to those of Co<sup>II</sup>.

At the Ni<sup>II</sup> L<sub>2,3</sub> edge, a shoulder is still observed on the main peak at the same energy as for **1**, but with weaker intensity. Good agreement between experimental spectra and LFM calculation is obtained by using 50% of Ni sites with

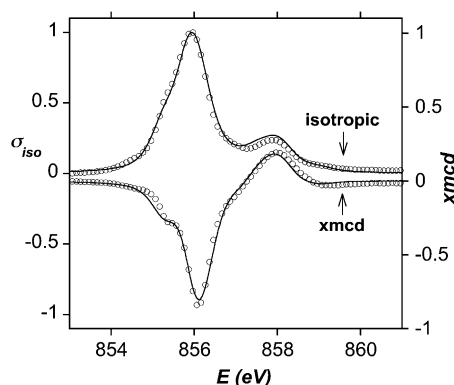


Figure 8. Experimental (○) and calculated (—) isotropic and XMCD spectra at the Ni<sup>II</sup> L<sub>3</sub> edge for **2**.

$D_{4h}$  symmetry instead of 70% for **1** (Figure 8). Thus, the number of distorted Ni<sup>II</sup> sites has been reduced from 70 to 50% in the core-shell structure. The 30% of distorted Ni<sup>II</sup> sites belonging to the volume of the core particles should remain unaffected in the core-shell nanoparticles. The 40% of Ni<sup>II</sup> sites belonging to the surface of the core particles are linked to the Cr(CN)<sub>6</sub><sup>3-</sup> ions of the shell in the core-shell objects, but only partially, because the shell network, like the core, has hexacyanochromate vacancies, as found by elemental analysis. This is why 20% of the Ni<sup>II</sup> sites present at the interface between the core and the shell still have a distorted environment, as depicted in Figure 9.

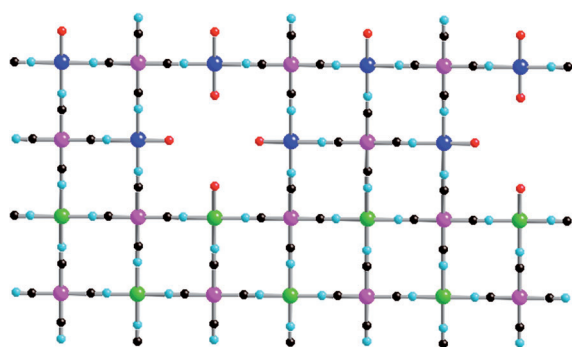


Figure 9. View of the interface of the core-shell particle with Cr(CN)<sub>6</sub> vacancies. N light blue, C black, Ni green, Cr pink, Co blue.

The LFM calculations for the Co<sup>II</sup> L<sub>2,3</sub> edge were performed by considering only  $O_h$  symmetry, because the spectrum is much more complex than that of Ni<sup>II</sup> and additional parameters may not give better insight into the nature of the different sites. The LFM calculations reproduce fairly well the features of the experimental spectrum (see Figure S6 in the Supporting Information); the small differences can be accounted for by the presence of distorted Co<sup>II</sup> sites (see Figure S6 in the Supporting Information), as in the case of Ni<sup>II</sup>. Indeed, since a shell thickness of 1 nm corresponds to two molecular layers (Figure 9), about 55% of Co<sup>II</sup> ions show a deviation from  $O_h$  symmetry. Moreover, the slight

difference in lattice parameters between the CsNi<sup>II</sup>Cr<sup>III</sup>(CN)<sub>6</sub> and the CsCo<sup>II</sup>Cr<sup>III</sup>(CN)<sub>6</sub> networks ( $\Delta a = 0.05$  Å) may induce distortion of the first coordination sphere of Co<sup>II</sup> ions located at the interface between the core and the shell, which leads to a deviation from  $O_h$  symmetry.

**Magnetization curves: variations of the Ni<sup>II</sup>, Co<sup>II</sup>, and Cr<sup>III</sup> local magnetic moments with magnetic field:** The magnetization curves of **2** obtained by XMCD at the Ni<sup>II</sup>, Co<sup>II</sup> and Cr<sup>III</sup> L<sub>2,3</sub> edges were normalized in the same manner as for **1** (Figure 10). In the case of Ni<sup>II</sup> edges, the proportions of

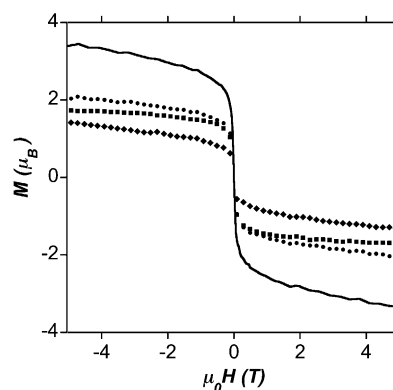


Figure 10. Local magnetization curves of **2** at 4.2 K at the Ni<sup>II</sup> (■), Co<sup>II</sup> (◆), and Cr<sup>III</sup> (●) L<sub>3</sub> edges and reconstruction of the total magnetization (—) considering the formula Ni<sup>II</sup><sub>0.51</sub>Co<sup>II</sup><sub>0.49</sub>[Cr<sup>III</sup>(CN)<sub>6</sub>]<sub>0.9</sub>.

these two symmetries  $O_h$  and  $D_{4h}$  were taken into account in the calculations to fit the XMCD spectra with the same set of parameters. For the Co<sup>II</sup> edges, only the  $O_h$  symmetry was used. The kinetic orbital momentum for the ground state of the simulated Co<sup>II</sup> ion is  $\langle L_z \rangle = -0.90$  and the kinetic spin momentum  $\langle S_z \rangle \approx -0.92$ .

The slope of the magnetization curves obtained from XMCD measurements clearly evidences that the Cr<sup>III</sup> ions display an intermediate behavior between Ni<sup>II</sup> and Co<sup>II</sup>, which is in line with the relative reduction factors needed to reproduce the intensity of the experimental XMCD spectra from calculations. The magnetic moment of Ni<sup>II</sup> is more saturated than that of Cr<sup>III</sup>, and the magnetic moment of Co<sup>II</sup> is less saturated (Figure 10). This is also in agreement with the values of the magnetization rates at 5 T of 76, 67, and 52% for the Ni<sup>II</sup>, Cr<sup>III</sup> and Co<sup>II</sup>, respectively, at the L<sub>2,3</sub> edges. The expected values for the magnetic moments at saturation, when full alignment with the field is assumed, are  $2.28\mu_B$  for Ni<sup>II</sup>,  $3\mu_B$  for Cr<sup>III</sup>, and  $2.74\mu_B$  for Co<sup>II</sup>.

In the core-shell particles, 55% of the Co<sup>II</sup> ions are located at the surface with symmetry lower than  $O_h$ . This leads to pronounced surface anisotropy, higher than that of Ni<sup>II</sup> in **1**, because of the near-first-order spin-orbit coupling expected for these slightly distorted Co<sup>II</sup> ions, which leads to deviation of the magnetic moment of the whole shell in a different direction from that of the CsNi<sup>II</sup>Cr<sup>III</sup>(CN)<sub>6</sub> core. The XMCD analysis leads to the conclusion that the Co<sup>II</sup> ions



are responsible for the large magnetic anisotropy observed for **2**. However, it is not possible to distinguish between the roles played by the Co<sup>II</sup> ions belonging to the surface and those present in the body of the shell, even though this is likely to be the case, since the atoms belonging to the surface are the more distorted. The answer to this important question was given recently when we compared the anisotropy between core-shell particles similar to those studied here and particles with a random distribution of Co<sup>II</sup> ions. The results obtained verify our hypothesis that the surface ions mainly contribute to the whole magnetic anisotropy.<sup>[17]</sup> As a consequence, the magnetic moments of the Cr<sup>III</sup> ions belonging to the shell are rather aligned with those of Co<sup>II</sup> because of the ferromagnetic interaction between these two ions.<sup>[45]</sup> On going deeper towards the center of the particle, the Cr<sup>III</sup> ions are less influenced by Co<sup>II</sup> but more by the less anisotropic Ni<sup>II</sup> ions. Indeed, the Cr<sup>III</sup> ions experience three different exchange fields and two anisotropy fields with different magnitudes. Those present on the surface (31 % of all Cr<sup>III</sup> ions) are coupled only to Co<sup>II</sup> and their moments are rather aligned with those of Co<sup>II</sup>. The Cr<sup>III</sup> ions present within the volume of the core (27 %) are exclusively coupled to the Ni<sup>II</sup> moments and are expected to be fully aligned with them, as shown by the value of the reduction coefficients found for **1**. The Cr<sup>III</sup> ions present at the interface between the core and the shell (42 % of the total amount of Cr<sup>III</sup> ions of the nanoparticle) feel an intermediate exchange field, since they interact with the Ni<sup>II</sup> and the Co<sup>II</sup> ions (Figure 9). Thus, the Cr<sup>III</sup> ions display a nonuniform magnetization, influenced by the anisotropy of divalent ions with which they are exchange-coupled. This accounts for the reduced magnetic saturation at the Cr edge for **2** ( $2.04\mu_B$ , i.e., 67 % of the magnetization) in comparison to **1** ( $2.33\mu_B$ , i.e., 78 % of the magnetization). Similarly, the Ni<sup>II</sup> ions present at the interface undergo an exchange coupling interaction with the Cr<sup>III</sup> ions belonging to the shell, which feel the influence of the large anisotropy of Co<sup>II</sup>; this is the origin of the slightly lower saturation magnetization value of Ni<sup>II</sup> in **2** than in **1**.

Finally, by taking into account the unit formula of  $\text{Ni}_{0.51}^{II}\text{Co}_{0.49}^{II}[\text{Cr}^{III}(\text{CN})_6]_{0.9}$  for **2**, the sum of the local magnetization curves led to the total magnetization curve as a function of the applied field (Figure 10). A magnetization of  $3.40\mu_B$  at 5 T was obtained, which differs from that of the SQUID data ( $4.07\mu_B$ ). This difference may have its origin in the XMCD technique, as already mentioned for **1**, XMCD is a surface-sensitive technique leading to weighted detection, so that the contribution of the surface of the particles is larger than that of the core. Since the highly anisotropic Co<sup>II</sup> ions are present on the surface, their larger contribution leads to underestimation of the magnetization. Indeed, the higher slope observed in the magnetization curve obtained by XMCD measurement is in good agreement with weighted detection.

## Conclusion

Studies by XAS and XMCD spectroscopy revealed two different environments around the Ni<sup>II</sup> ions in the 6 nm  $\text{CsNi}^{II}\text{Cr}^{III}(\text{CN})_6$  nanoparticles. The two coordination spheres,  $\text{Ni}^{II}(\text{NC})_6$  and  $\text{Ni}^{II}(\text{NC})_{6-x}(\text{OH}_2)_x$ , are respectively described through LFM calculations by  $O_h$  and  $D_{4h}$  symmetry. The results show that a part of the  $D_{4h}$  environment corresponds to surface ions, responsible for weak surface anisotropy. The presence of surface Ni<sup>II</sup> ions with uniaxial magnetic anisotropy accounts for the observed magnetic anisotropy. Probing the local magnetic moment of the Cr<sup>III</sup> ions allows the conclusion that their moments are aligned with the more anisotropic Ni<sup>II</sup> ions because of the exchange coupling interaction between the two metal ions. This is confirmed by the same values of the reduction coefficients found for **1** and is compatible with the superparamagnetic behavior and the presence of a defined blocking temperature observed for these 6 nm particles.<sup>[26]</sup> In the case of the core-shell nanoparticles, a unique magnetic behavior is observed despite the presence of two different networks, which is due to exchange coupling between the core and the shell. However, the dynamic susceptibility studies are not compatible with particles having a unique giant magnetic moment, as for **1**. Indeed, the interplay between the magnitude of the magnetic anisotropy and the exchange coupling energy between the core, the shell, and the interface imposes nonuniform magnetization throughout the nanoparticle, as accounted for from the experimental and the theoretical local XMCD studies. The presence of the anisotropic Co<sup>II</sup> ions at the surface and at the interface in addition to the exchange anisotropy associated with the core-shell architecture accounts for the larger magnetic anisotropy of these particles, which display a coercive field seven times larger than for the magnetically soft  $\text{CsNi}^{II}\text{Cr}^{III}(\text{CN})_6$  particles, as observed by SQUID studies.

## Experimental Section

**Preparation of 1:** The preparation of the 6 nm  $\text{CsNi}^{II}\text{Cr}^{III}(\text{CN})_6$  nanoparticles was already reported. Briefly, an aqueous solution (100 mL) of  $[\text{Ni}^{II}(\text{H}_2\text{O})_6]\text{Cl}_2$  (2 mM) and CsCl (4 mM) was added to 100 mL of an aqueous solution of  $\text{K}_3[\text{Cr}^{III}(\text{CN})_6]$  (2 mM) with vigorous stirring. The solution was stirred for 1 h and a DLS measurement made (see Supporting Information Figure S1). Then, a methanolic solution of three molar equivalents of dimethyldioctadecylammonium bromide (DODABr) was added to flocculate the nanoparticles. The colloidal solution was then centrifuged at 8000 rpm for 15 min and filtered. To remove the excess of DODABr, the powder was dispersed in a  $\text{CHCl}_3$ /pentane with stirring and then collected by centrifugation. The powder was dried under vacuum. Elemental analysis (%) calcd for  $\text{C}_{31.4}\text{H}_{60.16}\text{Cr}_{0.92}\text{Cs}_{0.51}\text{N}_{6.2}\text{NiO}_{2.88}$ : H 7.9, C 49.1, N 11.3, Cr 6.23, Ni 7.65, Cs 8.83; found: H 7.39, C 46.5, N 11.3, Cr 5.88, Ni 7.19, Cs 8.24. The formula of **1** is  $\text{Cs}_{0.51}\text{Ni}[\text{Cr}(\text{CN})_6]_{0.92} \cdot \{\text{DODA}\}_{0.25}\{\text{DODABr}\}_{0.17}\{\text{DODACl}\}_{0.26}(\text{H}_2\text{O})_{2.88}$  ( $M = 767 \text{ g mol}^{-1}$ ).

**Preparation of 2:** Solutions of  $[\text{Co}^{II}(\text{H}_2\text{O})_6]\text{Cl}_2$  (4 mM) and CsCl (8 mM) in water (150 mL) and of  $\text{K}_3[\text{Cr}^{III}(\text{CN})_6]$  (4 mM) in water (150 mL) were simultaneously added dropwise ( $1 \text{ mL s}^{-1}$ ) to 200 mL of an aqueous solution of 6 nm  $\text{CsNi}^{II}\text{Cr}^{III}(\text{CN})_6$  (before adding DODABr). The particle size was checked in situ by dynamic light scattering (see Supporting Informa-

tion Figure S1). The core-shell nanoparticles were flocculated with DODABr and then purified by following the same protocol as for **1**. Elemental analysis (%) calcd for  $C_{14.5}H_{24.6}Cr_{0.9}Cs_{0.6}N_{5.64}Ni_{0.51}Co_{0.49}O_{2.7}$ : H 4.83, C 34.0, N 15.4, Cr 9.11, Ni 5.83, Cs 15.5; found: H 5.16, C 35.5, N 15.5, Cr 9.57, Ni 6.11, Cs 16.4. The formula of **2** is  $Cs_{0.60}Ni_{0.51}Co_{0.49}[Cr(CN)_6]_{0.90}[DODA]_{0.1}[DODABr]_{0.04}[DODACl]_{0.1} \cdot [H_2O]_{2.70}$  ( $M = 513 \text{ g} \cdot \text{mol}^{-1}$ ).

**Dynamic light scattering:** The dynamic light scattering (DLS) measurements were performed on a Malvern Nanozetasizer Apparatus (equipped with a backscattering mode) on 1.5 mL of the particles dispersed in solution. The volume profile was used to estimate the size corresponding to the main peaks. This measurement was used as a qualitative measurement of the size of the particles or aggregates in solution, which systematically includes a solvation shell. It provides a comparative measurement to follow the growth of the multishell particles in solution.

**Transmission electron microscopy:** TEM measurements were done on a Philips EM208 TEM with 100 keV incident electrons focused on the specimen.

**Powder X-ray diffraction:** Powder XRD was performed on powders deposited on aluminum plate and recorded on a Philipps Panalytical X'Pert Pro MPD powder diffractometer with  $Cu_{K\alpha}$  radiation equipped with a fast detector.

**Magnetic measurements:** The magnetic measurements were performed with a Quantum Design MPMS-5S SQUID magnetometer for dc measurements. The field-dependent magnetization was measured at 2 K in the 0–5.5 kOe range. The ac data were collected on a Quantum Design MPMS-XL SQUID magnetometer working with an oscillating field of 3 Oe at six different frequencies in the range 1–1000 Hz.

**X-ray absorption and X-ray magnetic circular dichroism:** X-ray absorption near-edge structure and X-ray magnetic circular dichroism were recorded at the  $L_{2,3}$  edges of nickel and chromium for **1** and nickel, chromium, and cobalt for **2** on the SIM beamline at the Swiss Light Source (SLS) by using left and right circularly polarized light. The estimated circular polarization rate was 100%. The measurements were made at  $T = 4.2 \text{ K}$  with an applied field of 2 T parallel and antiparallel to the X-ray propagation vector, and the detection mode was total electron yield (TEY). The XMCD signal was obtained as the difference  $\sigma^- - \sigma^+$ , where  $\sigma^- = [\sigma_L(B^-) + \sigma_R(B^+)]/2$ ,  $\sigma^+ = [\sigma_L(B^+) + \sigma_R(B^-)]/2$ ,  $\sigma_L$  ( $\sigma_R$ ) is the cross-section with left (right) polarized X-rays, and  $B^+$  ( $B^-$ ) the magnetic field parallel (antiparallel) to the X-ray propagation vector. We did not observe any linear dichroism, so the isotropic spectrum is  $\sigma_{iso} = (\sigma^- + \sigma^+)/2$ . For comparison, the isotropic spectra were normalized to unity at the maximum of the  $L_3$  edge.

**Ligand field multiplet calculations:** The theoretical  $L_{2,3}$ -edge spectra were simulated by using the ligand field multiplet code developed by Thole<sup>[47]</sup> in the atomic and symmetry-adapted framework established by Cowan and Butler.<sup>[48–49]</sup> This approach takes into account the multielectronic Coulomb repulsions, the 3d and 2p spin-orbit coupling, and spin and orbit contributions to the Zeeman Hamiltonian and treats the geometric environment of the absorbing atom by an electrostatic potential.<sup>[50]</sup> The spectrum is calculated as the sum of all possible transitions between an atomic ground state configuration and all other atomic configurations with a core hole on the 2p level. The interaction Hamiltonian between X-ray and matter is written in the electric dipole approximation. Since the electric-dipole-allowed 2p to 4s transitions were calculated and found to be negligible, only 2p to 3d transitions were considered. Multielectronic Coulomb repulsions are modeled through the Slater integrals calculated within an atomic Hartree–Fock model and the Slater integrals are scaled down by a reduction factor  $\kappa$  to account for the electronic delocalization. The spin–orbit coefficients are the Hartree–Fock calculated ones. An octahedral ( $O_h$ ) or a tetragonal ( $D_{4h}$ ) electrostatic crystal field describes the coordination sphere of the absorbing ion. The calculated discrete line spectra are convolved with Gaussian function (half-width at half-maximum (HWHM)/eV =  $1.18\sigma$ ) for instrumental broadening and a Lorentzian function (HWHM =  $\Gamma$ ) with different widths  $\Gamma$  for  $L_3$  and  $L_2$  edges to account for super-Coster–Kronig transitions.

## Acknowledgements

We thank the Université Paris Sud 11, the CNRS (Centre National de la Recherche Scientifique), the French programme ANR-blanc (project MS-MCNP n°30615) for financial support.

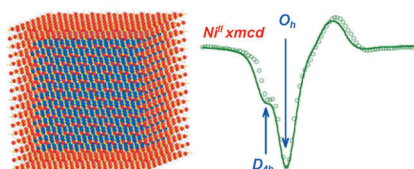
- [1] S. Vaucher, M. Li, S. Mann, *Angew. Chem.* **2000**, *112*, 1863; *Angew. Chem. Int. Ed.* **2000**, *39*, 1793.
- [2] S. Vaucher, J. Fielden, M. Li, E. Dujardin, S. Mann, *Nano Lett.* **2002**, *2*, 225.
- [3] L. Catala, C. Mathoniere, A. Gloter, O. Stephan, T. Gacoin, J. P. Boilot, T. Mallah, *Chem. Commun.* **2005**, 746.
- [4] L. Catala, A. Gloter, O. Stephan, G. Rogez, T. Mallah, *Chem. Commun.* **2006**, 1018.
- [5] G. Clavel, J. Larionova, Y. Guari, C. Guerin, *Chem. Eur. J.* **2006**, *12*, 3798.
- [6] Y. Guari, J. Larionova, K. Molvinger, B. Folch, C. Guerin, *Chem. Commun.* **2006**, 2613.
- [7] D. Brinzei, L. Catala, C. Mathoniere, W. Wernsdorfer, A. Gloter, O. Stephan, T. Mallah, *J. Am. Chem. Soc.* **2007**, *129*, 3778.
- [8] M. Arai, M. Miyake, M. Yamada, *J. Phys. Chem. C* **2008**, *112*, 1953.
- [9] L. Catala, F. Volatron, D. Brinzei, T. Mallah, *Inorg. Chem.* **2009**, *48*, 3360.
- [10] B. Folch, J. Larionova, Y. Guari, K. Molvinger, C. Luna, C. Sangregorio, C. Innocenti, A. Caneschi, C. Guerin, *Phys. Chem. Chem. Phys.* **2010**, *12*, 12760.
- [11] D. Brinzei, L. Catala, N. Louvain, G. Rogez, O. Stephan, A. Gloter, T. Mallah, *J. Mater. Chem.* **2006**, *16*, 2593.
- [12] L. Catala, D. Brinzei, Y. Prado, A. Gloter, O. Stéphan, G. Rogez, T. Mallah, *Angew. Chem.* **2009**, *121*, 189; *Angew. Chem. Int. Ed.* **2009**, *48*, 183.
- [13] E. E. Fullerton, J. S. Jiang, M. Grimsditch, C. H. Sowers, S. D. Bader, *Phys. Rev. B* **1998**, *58*, 12193.
- [14] J. Nogues, J. Sort, V. Langlais, V. Skumryev, S. Surinach, J. S. Munoz, M. D. Baro, *Phys. Rep.* **2005**, *422*, 65.
- [15] J. Sort, B. Dieny, J. Nogues, *Phys. Rev. B* **2005**, *72*, 104412.
- [16] J. Sort, F. Garcia, S. Auffret, B. Rodmacq, B. Dieny, V. Langlais, S. Surinach, J. S. Munoz, M. D. Baro, J. Nogues, *Appl. Phys. Lett.* **2005**, *87*, 242504.
- [17] Y. Prado, N. Dia, L. Lisnard, G. Rogez, F. Brisset, L. Catala, T. Mallah, *Chem. Commun.* **2012**, *48*, 11455.
- [18] G. Rogez, J. N. Rebilly, A. L. Barra, L. Sorace, G. Blondin, N. Kirchner, M. Duran, J. van Slageren, S. Parsons, L. Ricard, A. Marvilliers, T. Mallah, *Angew. Chem.* **2005**, *117*, 1910; *Angew. Chem. Int. Ed.* **2005**, *44*, 1876.
- [19] O. Kahn, *Molecular magnetism*, VCH Publishers Inc., New York, **1993**, p. 31.
- [20] S. Brice-Profeta, M. A. Arrio, E. Tronc, N. Menguy, I. Letard, C. Cartier dit Moulin, M. Nogues, C. Chaneac, J. P. Jolivet, P. Saintavrit, *J. Magn. Magn. Mater.* **2005**, *288*, 354.
- [21] L. Signorini, L. Pasquini, F. Boscherini, E. Bonetti, I. Letard, S. Brice-Profeta, P. Saintavrit, *Phys. Rev. B* **2006**, *74*, 014426.
- [22] D. H. Kim, H. J. Lee, G. Kim, Y. S. Koo, J. H. Jung, H. J. Shin, J. Y. Kim, J. S. Kang, *Phys. Rev. B* **2009**, *79*, 033402.
- [23] F. Jimenez-Villacorta, C. Prieto, Y. Huttel, N. D. Telling, G. van der Laan, *Phys. Rev. B* **2011**, *84*, 172404.
- [24] A. Ludi, H. U. Güdel, *Struct. Bonding (Berlin)* **1973**, *14*, 1–21.
- [25] M. Verdaguer, G. S. Girolami, “*Magnetic Prussian Blue Analogs*” in *Magnetism: Molecules to Materials V* (Ed.: J. S. Miller, M. Drillon), Wiley-VCH, Weinheim, **2005**.
- [26] Y. Prado, L. Lisnard, D. Heurtaux, G. Rogez, A. Gloter, O. Stephan, N. Dia, E. Riviere, L. Catala, T. Mallah, *Chem. Commun.* **2011**, *47*, 1051–1053.
- [27] B. Fleury, F. Volatron, L. Catala, D. Brinzei, E. Riviere, V. Huc, C. David, F. Miserque, G. Rogez, L. Baraton, S. Palacin, T. Mallah, *Inorg. Chem.* **2008**, *47*, 1898.
- [28] M. A. Arrio, P. Saintavrit, C. Cartier dit Moulin, C. Brouder, F. M. F. de Groot, T. Mallah, M. Verdaguer, *J. Phys. Chem.* **1996**, *100*, 4679.

- [29] Since the elemental analysis of **1** gave a unit formula with 1 Ni<sup>II</sup> ( $S=1$ ) and 0.92 Cr<sup>III</sup> ( $S=3/2$ ) ions, a value of  $4.95\mu_B$  is computed assuming  $g_{Ni}=2.2$  and  $g_{Cr}=1.99$ .
- [30] V. Gadet, T. Mallah, I. Castro, M. Verdaguer, P. Veillet, *J. Am. Chem. Soc.* **1992**, *114*, 9213.
- [31] T. Mallah, C. Auberger, M. Verdaguer, P. Veillet, *J. Chem. Soc. Chem. Commun.* **1995**, 61.
- [32] T. Mallah, S. Ferlay, C. Auberger, C. Helary, F. L'Hermite, R. Ouahes, J. Vaissermann, M. Verdaguer, P. Veillet, *Mol. Cryst. Liq. Cryst. Sci. Technol. Sect. A* **1995**, *273*, 141.
- [33] M. A. Arrio, P. Saintavit, C. Cartier dit Moulin, T. Mallah, M. Verdaguer, E. Pellegrin, C. T. Chen, *J. Am. Chem. Soc.* **1996**, *118*, 6422.
- [34] A. Flambard, F. H. Kohler, R. Lescouezec, *Angew. Chem.* **2009**, *121*, 1701; *Angew. Chem. Int. Ed.* **2009**, *48*, 1673.
- [35] A. Flambard, F. H. Kohler, R. Lescouezec, B. Revel, *Chem. Eur. J.* **2011**, *17*, 11567.
- [36] Strictly, the Ni(NC)<sub>5</sub>(H<sub>2</sub>O) site is  $C_{4v}$ -symmetric but can reasonably be assumed to have  $D_{4h}$  symmetry. The Ni(NC)<sub>4</sub>(H<sub>2</sub>O)<sub>2</sub> sites can be *trans* or *cis*, and only the *trans* isomer is  $D_{4h}$ -symmetric. The Ni(NC)<sub>5</sub>(H<sub>2</sub>O)<sub>3</sub> sites make a negligible contribution. Since the sites with  $C_{4v}$  and  $D_{4h}$  symmetry account for more than 80% of the total distorted sites (see Supporting Information), our assumption that the distorted sites are  $D_{4h}$ -symmetric is reasonable in this context.
- [37] A. B. P. Lever, *Inorganic Electronic Spectroscopy*, Elsevier, Amsterdam, **1984**, p. 511.
- [38] A. Abragam, B. Bleaney, *Electron Paramagnetic Resonance of Transition Ions*, Oxford University Press, Oxford, **1986**.
- [39] G. Rogez in *Modulation des propriétés électroniques et de l'anisotropie magnétique de complexes mono et polynucléaires: influence des ligands pontants et périphériques*, PhD thesis. Université Paris Sud 11, **2002**, p. 400.
- [40] J. N. Rebilly, L. Catala, G. Charron, G. Rogez, E. Riviere, R. Guillet, P. Thuery, A. L. Barra, T. Mallah, *Dalton Trans.* **2006**, 2818.
- [41] A small number of these Ni<sup>II</sup> surface sites may have two water molecules in *cis* position, and in this case the easy axis of magnetization will not be normal to the surface.
- [42] J. L. Dormann, L. Bessais, D. Fiorani, *J. Phys. C Solid State* **1988**, *21*, 2015.
- [43] J. L. Dormann, F. D'Orazio, F. Lucari, E. Tronc, P. Prene, J. P. Jolivet, D. Fiorani, R. Cherkaoui, M. Nogues, *Phys. Rev. B* **1996**, *53*, 14291.
- [44] S.-i. Ohkoshi, T. Iyoda, A. Fujishima, K. Hashimoto, *Phys. Rev. B* **1997**, *56*, 11642.
- [45] S. Ohkoshi, K. Hashimoto, *Chem. Phys. Lett.* **1999**, *314*, 210.
- [46] S. Ferlay, T. Mallah, R. Ouahes, P. Veillet, M. Verdaguer, *Inorg. Chem.* **1999**, *38*, 229.
- [47] B. T. Thole, G. Vanderlaan, J. C. Fuggle, G. A. Sawatzky, R. C. Karnatak, J. M. Esteve, *Phys. Rev. B* **1985**, *32*, 5107.
- [48] R. D. Cowan, *The Theory of Atomic Structure and Spectra*, University of California Press, Berkeley, **1981**.
- [49] P. H. Butler, *Point Group Symmetry, Applications, Methods and Tables*, Plenum, New York, **1991**.
- [50] F. M. F. de Groot, J. C. Fuggle, B. T. Thole, G. A. Sawatzky, *Phys. Rev. B* **1990**, *42*, 5459.

Received: October 9, 2012

Published online: ■ ■ ■, 0000

**Two different Ni<sup>II</sup> environments** in 6 nm-sized, bimetallic, CsNiCr(CN)<sub>6</sub> nanoparticles and 8 nm-sized, trimetallic, CsNiCr(CN)<sub>6</sub>@CsCoCr(CN)<sub>6</sub> core-shell nanoparticles were revealed by X-ray magnetic circular dichroism (XMCD). The experimental XMCD spectrum could be reproduced by ligand-field multiplet calculations assuming Ni<sup>II</sup>(NC)<sub>6</sub> and Ni<sup>II</sup>(NC)<sub>6-x</sub>(OH<sub>2</sub>)<sub>x</sub> coordination spheres with *O<sub>h</sub>* and *D<sub>4h</sub>* symmetry, respectively (see figure).



## Coordination Nanoparticles

Y. Prado,\* M.-A. Arrio,\* F. Volatron,  
E. Otero, C. Cartier dit Moulin,  
P. Sainctavit, L. Catala,  
T. Mallah\* ..... ■■■-■■■

**Magnetic Anisotropy of Cyanide-Bridged Core and Core-Shell Coordination Nanoparticles Probed by X-ray Magnetic Circular Dichroism**

